614 *Inorg. Chem.* **2011**, *50*, 614–620
DOI: 10.1021/ic101730r

Inorganic Chemistry
Article

XAS and DFT Investigation of Mononuclear Cobalt(III) Peroxo Complexes: Electronic Control of the Geometric Structure in CoO_2 versus NiO_2 Systems

Ritimukta Sarangi,*,[†] Jaeheung Cho,[‡] Wonwoo Nam,[‡] and Edward I. Solomon*,[†,§]

[†] *Stanford Synchrotron Radiation Lightsource, SLAC National Accelerator Laboratory, Menlo Park, California 94025, United States ,* [‡] *Department of Chemistry and Nano Science, Department of Bioinspired Science, Center for Biomimetic Systems, Ewha Woman's University, Seoul 120-750, Korea, and* [§] *Department of Chemistry, Stanford University, Stanford, California 94305, United States*

Received August 25, 2010

The geometric and electronic structures of two mononuclear $[(L)CoO_2]^+$ complexes, $[(12\text{-TMC})CoO_2](ClO_4)$ (**1**) and $[(14\text{-TMC})CoO_2](ClO_4)$ (**2**), have been evaluated using Co K-edge X-ray absorption spectroscopy (XAS) and extended X-ray absorption fine structure (EXAFS) and correlated with density functional theory (DFT) calculations to evaluate the differences in the geometric and electronic structures due to changes in the TMC chelate ring size. Co K-edge XAS shows that both **1** and **2** are Co^{III} species. Co K-edge EXAFS data show that both **1** and **2** are side-on O_2-bound cobalt(III) peroxide complexes. A combination of EXAFS and DFT calculations reveals that while the constrained 12-TMC ring in **1** allows for side-on O_2 binding to the Co center with ease, the 14-TMC chelate in **2** has to undergo significant distortion of the ring to overcome steric hindrance posed by the four *cis*-methyl groups of the chelate to allow side-on O_2 binding to the Co center. The Ni analogue of **2**, $[(14\text{-TMC})NiO_2]^+$, has been shown to form an end-on-bound nickel(II) superoxide species. The electronic and geometric factors that determine the different electronic structures of **2** and $[(14\text{-TMC})NiO_2]^+$ are evaluated using DFT calculations. The results show that while the sterics of the *cis*-14-TMC chelate contribute to the geometry of O_2 binding and result in an end-on-bound $Ni^{II}O_2^-$ complex in $[(14\text{-TMC})NiO_2]^+$, the higher thermodynamic driving force for oxidation of Co^{II} overcomes this steric constraint, resulting in stabilization of a side-on-bound $Co^{III}O_2^{2-}$ electronic structure in **2**.

1. Introduction

Transition-metal active sites of proteins play vital roles in dioxygen binding and reduction in a variety of important biological processes because they facilitate the spin-forbidden interaction between dioxygen and organic matter.[1−4] Understanding the mechanism of dioxygen binding and the geometric and electronic structures of the various intermediates generated in the process of dioxygen activation is of key importance in understanding the overall reaction mechanism of metalloproteins. In the case of mononuclear dioxygen-activating proteins, the first step involves the formation of a $M-O_2$ (M = metal active site) intermediate, which can either react directly or lead to the formation of a high-valent metal−oxo intermediate. This $M-O_2$ intermediate can potentially assume different O_2 binding modes (side-on or end-on), different oxidation states (O_2, O_2^-, or O_2^{2-}), different spin states at the metal center, and different exchange stabilizations between the dioxygen moiety and the metal center. Biomimetic efforts have resulted in the synthesis of various $M-O_2$ ($M-O$) intermediates,[5−8] and spectroscopic characterization of these intermediates has been directed toward understanding factors that determine their electronic structure, which can make a key contribution to the reactivity.

Macrocyclic tetradentate N_4 ligands, such as 1,4,8,11-tetramethyl-1,4,8,11-tetraazacyclotetradecane (14-TMC), have been effectively used in the synthesis of mononuclear $M-O$ complexes (M = Cr, Mn, Fe, and Ni).[9−13] Recently, we have

---

*To whom correspondence should be addressed. E-mail: edward.solomon@stanford.edu (E.I.S.), ritis@slac.stanford.edu (R.S.).

[1] Solomon, E. I.; Sarangi, R.; Woertink, J. S.; Augustine, A. J.; Yoon, J.; Ghosh, S. *Acc. Chem. Res.* **2007**, *40*, 581–591.

[2] Solomon, E. I.; Brunold, T. C.; Davis, M. I.; Kemsley, J. N.; Lee, S. K.; Lehnert, N.; Neese, F.; Skulan, A. J.; Yang, Y. S.; Zhou, J. *Chem. Rev.* **2000**, *100*, 235–350.

[3] Kovaleva, E. G.; Lipscomb, J. D. *Nat. Chem. Biol.* **2008**, *4*, 186–193.

[4] Hersleth, H. P.; Ryde, U.; Rydberg, P.; Gorbitz, C. H.; Andersson, K. K. *J. Inorg. Biochem.* **2006**, *100*, 460–476.

[5] Costas, M.; Mehn, M. P.; Jensen, M. P.; Que, L., Jr. *Chem. Rev.* **2004**, *104*, 939–986.

[6] Lewis, E. A.; Tolman, W. B. *Chem. Rev.* **2004**, *104*, 1047–1076.

[7] Nam, W. *Acc. Chem. Res.* **2007**, *40*, 522–531.

[8] Hatcher, L. Q.; Karlin, K. D. *J. Biol. Inorg. Chem.* **2004**, *9*, 669–683.

[9] Kieber-Emmons, M. T.; Annaraj, J.; Seo, M. S.; Van Heuvelen, K. M.; Tosha, T.; Kitagawa, T.; Brunold, T. C.; Nam, W.; Riordan, C. G. *J. Am. Chem. Soc.* **2006**, *128*, 14230–14231.

[10] Cho, J.; Woo, J.; Nam, W. *J. Am. Chem. Soc.* **2010**, *132*, 5958–5959.

[11] Cho, J.; Sarangi, R.; Annaraj, J.; Kim, S. Y.; Kubo, M.; Ogura, T.; Solomon, E. I.; Nam, W. *Nat. Chem.* **2009**, *1*, 568–572.

[12] Annaraj, J.; Suh, Y.; Seo, M. S.; Kim, S. O.; Nam, W. *Chem. Commun.* **2005**, 4529–4531.

[13] Seo, M. S.; Kim, J. Y.; Annaraj, J.; Kim, Y.; Lee, Y. M.; Kim, S. J.; Kim, J.; Nam, W. *Angew. Chem., Int. Ed.* **2007**, *46*, 377–380.

successfully synthesized Ni$-$O$_2$ complexes with a variety of different TMC ligands,[9,11] in which the ligand is varied from a 12-membered to a 14-membered ring (i.e., 12-TMC to 14-TMC; 12-TMC = 1,4,7,10-tetramethyl-1,4,7,10-tetraazacyclododecane). X-ray absorption spectroscopy (XAS) studies and density functional theory (DFT) calculations on [(12-TMC)NiO$_2$]$^+$ and [(14-TMC)NiO$_2$]$^+$ have revealed differences in the electronic and geometric structures that are associated with large steric hindrance posed by the 14-TMC ring bound to the Ni center with all four methyl groups cis to the O$_2$ binding side (Scheme 1). These differences translate to reactivity differences; while [(12-TMC)NiO$_2$]$^+$ (side-on-bound Ni^{III}O$_2$$^{2-}$) participates in nucleophilic reactions (aldehyde oxidation), [(14-TMC)NiO$_2$]$^+$ (end-on-bound Ni^{II}O$_2$$^-$) is capable of conducting electrophilic oxidative reactions.[11]

LCoO$_2$ complexes are important analogues of biological dioxygen carriers and have been synthesized with porphyrin, salen, and N$_4$ macrocyclic ligands.[14-16] We have extended these synthetic efforts toward cobalt complexes to characterize the reactivity differences of the [(TMC)CoO$_2$]$^+$ complexes with changes in the macrocycle ring size.[17] In a recent crystal structure of [(12-TMC)CoO$_2$]$^+$ (**1**), we have shown a side-on binding mode of the O$_2$ moiety to the Co center (Scheme 1) and showed that **1** is electron paramagnetic resonance (EPR) silent. Resonance Raman (rR) data revealed an O$-$O stretching frequency of 902 cm^{-1}, and Evan's method analysis of the NMR data shows that **1** has no unpaired electrons. Together, these data indicate a ground state that is consistent with a $S_{\text{total}} = 0$ Co^{III}O$_2$$^{2-}$ assignment of **1**. [(14-TMC)CoO$_2$]$^+$ (**2**) has also been synthesized; while no crystal structure or rR data have been accessible, Evan's method analysis of the NMR data revealed the presence of an unpaired spin on the Co center.

In this study, the differences in the electronic and geometric structures between **1** and **2** have been investigated using a combination of Co K-edge XAS, extended X-ray absorption fine structure (EXAFS), and DFT calculations. The factors that lead to the differences in the magnetic properties of the two complexes have been evaluated. The role of the macrocyclic ligands in determining the geometric and electronic structures of the Co complexes is evaluated and compared and contrasted to its effects on the [(TMC)NiO$_2$]$^+$ complexes. These studies reveal an interplay of the contributions from steric effects, bonding interaction, and the preferential stability of different oxidation states in determining the final electronic and geometric structures.

2. Experimental Section

2.1. Sample Preparation. [Co(12-TMC)O$_2$](ClO$_4$) (**1**),[17] [Co(14-TMC)O$_2$](ClO$_4$) (**2**),[18] [Co(12-TMC)(CH$_3$CN)](ClO$_4$)$_2$ (**1$_{\text{pre}}$**, precursor of **1**)[17] and [Co(14-TMC)(CH$_3$CN)](ClO$_4$)$_2$ (**2$_{\text{pre}}$**, precursor of **2**)[18] were synthesized as previously described. ***Caution!*** *Perchlorate salts are potentially explosive and should be handled with care!* Because both **1** and **2** are thermally unstable, care was taken to minimize decomposition during loading of the samples into the XAS cells and the loading time was minimized. Lucite XAS cells (2 mm) were used with 37 μm Kapton windows for the solution samples of **1** and **2**. The solid samples for **1$_{\text{pre}}$** and **2$_{\text{pre}}$** were finely ground with BN into a homogeneous mixture and pressed into a 1 mm aluminum spacer between 37 μm Kapton windows. The samples were immediately frozen and stored under liquid-N$_2$ conditions. During data collection, the samples were maintained at a constant temperature of ~10 K using an Oxford Instruments CF 1208 liquid-helium cryostat.

Scheme 1. Geometric Structures of [Ni(12-TMC)O$_2$]$^+$ (Crystal Structure), [Ni(14-TMC)O$_2$]$^+$ (Obtained from a Combination of Spectroscopic Techniques and DFT Calculations), and [Co(12-TMC)O$_2$]$^+$ (Crystal Structure)[a]

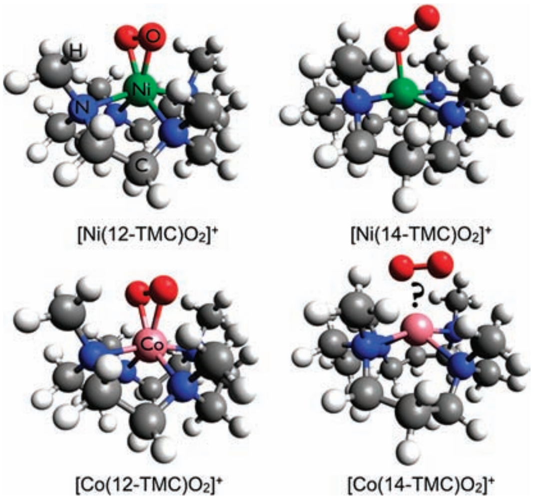

[a] The structure of [Co(14-TMC)O$_2$]$^+$ has not been accessible via X-ray diffraction. Color code: Ni, green; Co, pink; O, red; N, blue; C, gray; H, white.

2.2. XAS. Co K-edge XAS data were measured on the frozen samples of both the oxygenated complexes, **1** and **2**, and their Co^{II} precursors, **1$_{\text{pre}}$** and **2$_{\text{pre}}$**, on the 16-pole, 2-T wiggler beamline 9-3 at the Stanford Synchrotron Radiation Lightsource (SSRL) under standard ring conditions of 3 GeV and 100 mA ring current. A Si(220) double-crystal monochromator was used for energy selection. Other optical components used for the experiments were a Rh-coated harmonic rejection mirror and a cylindrical Rh-coated bent-focusing mirror. Data on **1** and **2** were measured in the fluorescence mode using a Canberra 30-element solid-state Ge detector. Data on **1$_{\text{pre}}$** and **2$_{\text{pre}}$** were measured in the transmission mode using an ionization chamber placed after the sample. Internal energy calibration was accomplished by the simultaneous measurement of the absorption of a Co foil placed between two ionization chambers situated after the sample. The first inflection point of the foil spectrum was fixed at 7709.5 eV. The samples were monitored for the potential signs of photoreduction throughout the course of data collection. To minimize the effect of beam damage and photoreduction, data were collected on an unexposed region of the sample cell after every four scans. Data presented here are eight-scan average spectra for both **1** and **2**, a six-scan average spectrum for **1$_{\text{pre}}$**, and a four-scan average spectrum for **2$_{\text{pre}}$**. The data were processed by fitting a second-order polynomial to the pre-edge region and subtracting this from the entire spectrum as the background. A three-region spline of orders 2, 3, and 3 was used to model the smoothly decaying post-edge region. The data were normalized in the *Pyspline* program[19] by subtracting the cubic spline and assigning the edge jump to 1.0 at 7730 eV.

---

(14) Hikichi, S.; Akita, M.; Moro-Oka, Y. *Coord. Chem. Rev.* **2000**, *198*, 61–87.

(15) Degtyarenko, I.; Nieminen, R. M.; Rovira, C. *Biophys. J.* **2006**, *91*, 2024–2034.

(16) Norman, J. A.; Pez, G. P.; Roberts, D. A. In *Oxygen Complexes and Oxygen Activation by Transition Metals*; Martell, A. E., Sawyer, D. T., Eds.; Plenum Press: New York, 1988.

(17) Cho, J.; Sarangi, R.; Kang, H. Y.; Lee, J. Y.; Kubo, M.; Ogura, T.; Solomon, E. I.; Nam, W. **2010**, submitted for publication.

(18) Jo, Y.; Annaraj, J.; Seo, M. S.; Lee, Y. M.; Kim, S. Y.; Cho, J.; Nam, W. *J. Inorg. Biochem.* **2008**, *102*, 2155–2159.

(19) Tenderholt, A. *Pyspline and QMForge*; 2007.

Theoretical EXAFS signals $\chi(k)$ were calculated by using *FEFF* (Macintosh version 8.4),[20–22] the crystal structures of **1**, **1**$_{\mathbf{pre}}$, and **2**$_{\mathbf{pre}}$, and a structural model of **2** based on the DFT geometry-optimized structure (see section 2.3). The theoretical models were fit to the data using *EXAFSPAK*.[23] The structural parameters varied during the fitting process were the bond distance (R) and the bond variance σ^2, which is related to the Debye−Waller factor resulting from thermal motion, and the pairwise static disorder of the absorbing and scattering atoms. The nonstructural parameter E_0 (the energy at which $k = 0$) was also allowed to vary but was restricted to a common value for every component in a given fit. The S_0^2 value was set at 0.8 for the entire course of the fit. Coordination numbers were systematically varied in the course of the fit but were fixed within a given fit.

2.3. Electronic Structure Calculations. Gradient-corrected, spin-unrestricted, broken-symmetry, DFT calculations were carried out using the *ORCA* package[24,25] on an 8-CPU linux cluster. The Becke88[26,27] exchange and Perdew86[28] correlation nonlocal functionals were employed to compare the differences between the electronic and geometric structures of **1** and **2**. The coordinates obtained from the crystal structure of **1** were used as the starting input structure for **1**. For **2**, the crystal structure of a monomeric $[Co(14\text{-}TMC)(acac)]^{3+}$ species[29] was modified to a $[Co(14\text{-}TMC)O_2]^+$ starting input structure. The core properties basis set CP(PPP) (as implemented in *ORCA*)[24,30] was used on Co, and Ahlrichs' all-electron triple-ζ TZVP[31,32] basis set was used on all other atoms. A tight convergence criterion was selected. Population analyses were performed by means of Mulliken Population Analysis. Wave functions were visualized, and orbital contour plots were generated in *Molden*.[33] Compositions of molecular orbitals and overlap populations between molecular fragments were calculated using *QMForge*.[19]

3. Results and Analysis

3.1. Co K-Edge XAS. The normalized Co K-edge XAS spectra of **1** and **1**$_{\mathbf{pre}}$ are shown in Figure 1A. The inset shows the expanded pre-edge region. The pre-edge feature occurs because of a quadrupole-allowed, dipole-forbidden Co 1s → 3d transition and is a measure of the ligand field strength at the metal center.[34−36] As seen from Figure 1, on going from **1**$_{\mathbf{pre}}$ to **1**, the pre-edge energy position shifts from 7709.2 to 7710.1 eV, indicating an increase in the ligand field strength in **1**. The edge region (∼7715−7725 eV) occurs because of the dipole-allowed Co 1s → 4p + continuum transition, and relative shifts in the edge energy position reflect the change in the charge at the Co center (Q_{Co}). Furthermore, additional transitions in the rising edge can occur because of charge-transfer shakeup processes or multiple scattering effects.[37−40] In **1**, the edge energy shifts up by ∼1.3 eV (relative to **1**$_{\mathbf{pre}}$) to 7720.6 eV, indicating an increase in Q_{Co}. This comparison of the Co K-edge XAS data of **1** with its Co^{II} precursor **1**$_{\mathbf{pre}}$ indicates that **1** is a one-electron-oxidized Co^{III} species with an increased ligand field strength. The edge shift combined with rR data,[17] which show an O−O stretching frequency of 902 cm^{-1} in **1**, indicate a cobalt(III) peroxide electronic structure with the peroxide bound in a side-on fashion to the Co^{III}. The crystal structure of **1** reveals a six-coordinate active site, in contrast to the five-coordinate site in **1**$_{\mathbf{pre}}$. The higher coordination number in **1** leads to an increased ligand field strength and is consistent with the ∼0.9 eV pre-edge shift to higher energy.[41]

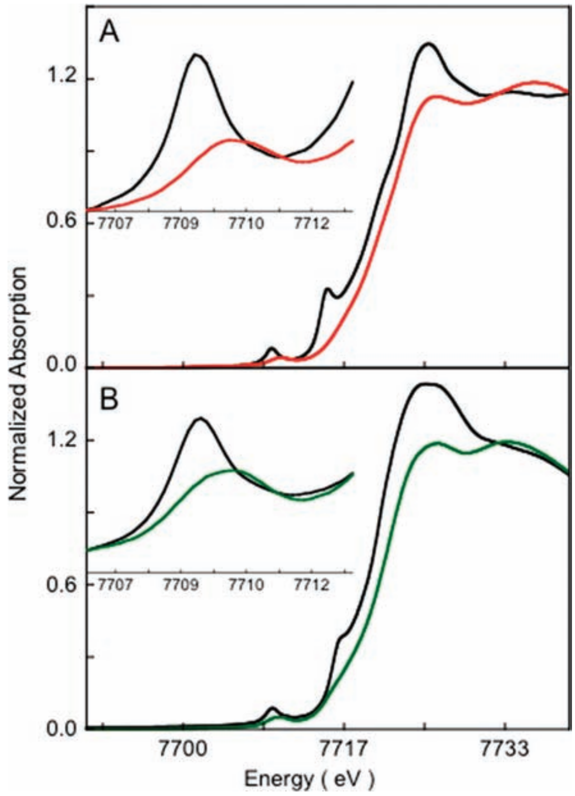

Figure 1. Normalized Co K-edge XAS spectra: (A) **1** (red line) and **1**$_{\mathbf{pre}}$ (black line); (B) **2** (green line) and **2**$_{\mathbf{pre}}$ (black line). The insets show the expanded pre-edge regions.

The normalized Co K-edge XAS spectra of **2** and **2**$_{\mathbf{pre}}$ are shown in Figure 1B. The inset shows the expanded

---

(20) Rehr, J. J.; Mustre de Leon, J.; Zabinsky, S. I.; Albers, R. C. *J. Am. Chem. Soc.* **1991**, *113*, 5135–5140.

(21) Rehr, J. J.; Albers, R. C. *Rev. Mod. Phys.* **2000**, *72*, 621–654.

(22) Mustre de Leon, J.; Rehr, J. J.; Zabinsky, S. I.; Albers, R. C. *Phys. Rev. B* **1991**, *44*, 4146–4156.

(23) George, G. N. *EXAFSPAK and EDG-FIT*; 2000.

(24) Neese, F.; Olbrich, G. *Chem. Phys. Lett.* **2002**, *362*, 170–178.

(25) Neese, F. *ORCA: an ab initio, DFT and semiempirical Electronic Structure Package*, version 2.4, revision 16; 2004.

(26) Becke, A. D. *J. Chem. Phys.* **1993**, *98*, 5648–5652.

(27) Becke, A. D. *Phys. Rev. A* **1988**, *38*, 3098–3100.

(28) Perdew, J. P. *Phys. Rev. B* **1986**, *33*, 8822–8824.

(29) Simon, E.; L'Haridon, P.; Pichon, R.; L'Her, M. *Inorg. Chim. Acta* **1998**, *282*, 173–179.

(30) Sinnecker, S.; Slep, L. D.; Bill, E.; Neese, F. *Inorg. Chem.* **2005**, *44*, 2245–2254.

(31) Schaefer, A.; Huber, C.; Ahlrichs, R. *J. Chem. Phys.* **1994**, *100*, 5829–5835.

(32) Schaefer, A.; Horn, H.; Ahlrichs, R. *J. Chem. Phys.* **1992**, *97*, 2571–2577.

(33) Schaftenaar, G.; Noordik, J. H. *J. Comput.-Aided Mol. Des.* **2000**, *14*, 123–134.

(34) Westre, T. E.; Kennepohl, P.; DeWitt, J. G.; Hedman, B.; Hodgson, K. O.; Solomon, E. I. *J. Am. Chem. Soc.* **1997**, *119*, 6297–6314.

(35) Penner-Hahn, J. E.; Scott, R. A.; Hodgson, K. O.; Doniach, S.; Desjardins, S. R.; Solomon, E. I. *Chem. Phys. Lett.* **1982**, *88*, 595–598.

(36) Shulman, R. G.; Yafet, Y.; Eisenberger, P.; Blumberg, W. E. *Proc. Natl. Acad. Sci. U.S.A.* **1976**, *73*, 1384–1388.

(37) Kosugi, N.; Yokoyama, T.; Asakura, K.; Kuroda, H. *Chem. Phys.* **1984**, *91*, 249–256.

(38) Frank, P.; Benfatto, M.; Hedman, B.; Hodgson, K. O. *Inorg. Chem.* **2008**, *47*, 4126–4139.

(39) Bair, R. A.; Goddard, W. A. *Phys. Rev. B* **1980**, *22*, 2767–2776.

(40) An edge transition is observed at 7714.9 eV in **3** and at 7116.2 eV in **4**, which can be attributed to multiple-scattering contributions from the linear MeCN group.

(41) Sarangi, R.; Aboelella, N.; Fujisawa, K.; Tolman, W. B.; Hedman, B.; Hodgson, K. O.; Solomon, E. I. *J. Am. Chem. Soc.* **2006**, *128*, 8286–8296.

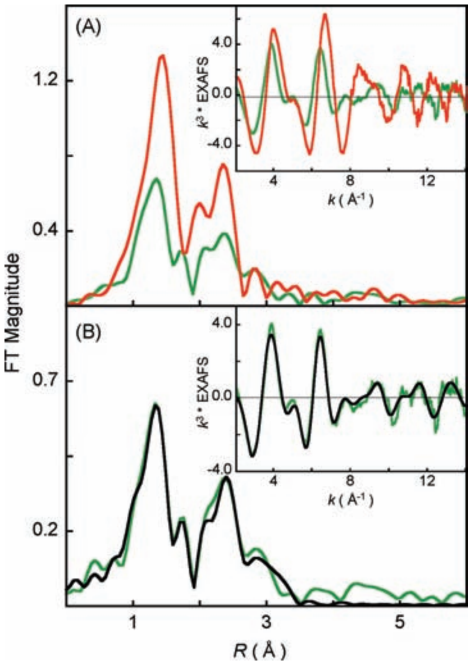

Figure 2. (A) Comparison of the nonphase-shift-corrected Fourier transforms for **1** (red line) and **2** (black lone). The inset shows the EXAFS comparison. (B) *FEFF* best-fit results for **2**: data (green line); fit (black line).

pre-edge region. The trend on going from $\mathbf{2_{pre}}$ to **2** is similar to that observed on going from $\mathbf{1_{pre}}$ to **1**; the pre-edge energy position shifts from 7709.3 to 7710.1 eV, indicating an increase in the ligand field strength in **2**. The edge position shifts up from 7719.1 eV in $\mathbf{2_{pre}}$ to 7720.4 eV in **2**, indicating an increase in Q_{Co} on **2**. This increase in the edge energy position indicates that **2** is a one-electron-oxidized species relative to $\mathbf{2_{pre}}$ and is also best described as a Co^{III} complex.

3.2. Co K-Edge EXAFS. Figure 2A shows a comparison of the nonphase-shift-corrected Fourier transforms for **1** and **2**. The inset shows the EXAFS comparison. The EXAFS analysis of **1** has been published elsewhere,[17] and the best fit is reproduced in Table 1 for comparison. The comparison shows that, on going from **1** to **2**, the EXAFS intensity decreases dramatically with a concomitant decrease in the first-shell intensity of the Fourier transforms. Additionally, the first shell in **2** splits, and a peak is observed at 1.7 Å (nonphase-shift-corrected). The second-shell intensity decreases almost 2-fold relative to that in **1**. The best fit to the EXAFS data for **2** is shown in Figure 2B and Table 1. The first shell was fit with two Co−O components at 1.88 Å and two Co−N components at 2.10 Å. Attempts to fit the data with two additional Co−N components, either at the same distance (2.10 Å) or at longer distances, were unsuccessful. The second shell was fit with single- and multiple-scattering contributions from Co−C (2.9 Å) and the corresponding Co−C−N (3.15 Å) shells. A third shell was required to fit the data with Co−C (3.5 Å) and Co−C−N (3.6 Å) shells. The presence of only two short Co−N distances and the requirement of third-shell single- and multiple-scattering components indicate the elongation of two Co−N bonds to significantly longer distances in **2** such that the single-scattering component is not required but the combined single and multiple scattering from the ring carbons, which is stronger, is required in the best fit. Thus, the EXAFS data reveal that the 14-TMC ring of **2** has undergone significant distortion with two elongated Co−N distances (evidenced by the presence of long-distance multiple scattering), two short Co−N distances, and two shorter Co−O distances. In contrast, the EXAFS data and the crystal structure of **1** reveal that the active site has two short Co−O bonds (~1.85 Å) and four similar Co−N bonds (~2.0 Å).

Table 1. EXAFS Least-Squares-Fitting Results

complex	coordination/path	R (Å)[a]	σ^2(Å^2)[b]	E_0 (eV)	F[c]
1	2 Co−O	1.85	323	1.81	0.16
	4 Co−N	1.99	317		
	8 Co−C[d]	2.84	393		
	24 Co−C−N[d]	3.14	382		
2	2 Co−O	1.88	341	2.91	0.08
	2 Co−N	2.10	530		
	4 Co−C[d]	2.90	853		
	8 Co−C−N[d]	3.16	853		
	4 Co−C−N[e]	3.52	628		
	12 Co−C−N[e]	3.57	224		

[a] The estimated standard deviations for the distances are on the order of ±0.02 Å. [b] The σ^2 values are multiplied by 10^5. [c] Error is given by $\sum[(\chi_{obsd} - \chi_{calcd})^2k^6]/\sum[(\chi_{obsd})^2k^6]$. [d] The single- and multiple-scattering contributions from the C atoms adjacent to the two 2.10 Å N atoms. [e] The longer-distance single- and multiple-scattering distances were required to fit the outer shell of the Fourier transform.

3.3. DFT Calculations. 3.3.1. $[(12\text{-TMC})CoO_2]^+$. Spin-unrestricted DFT calculations were performed on the $[(12\text{-TMC})CoO_2]^+$ moiety obtained from the crystal structure of **1**. $[(12\text{-TMC})CoO_2]^+$ can potentially exist in 14 different geometric and electronic configurations: either the end-on or side-on binding mode for O_2 in combination with $S = 0, 1$, or 2 spin states at the Co center and $S = {}^1/_2$ or 0 on O_2.[42] Geometry optimizations were performed, allowing for calculations to converge to all 14 configurations, out of which six different electronic configurations were achieved. These six configurations were compared to investigate differences in bonding and energy. The energies and structural parameters are given in Table 2. The calculations show that the side-on-bound $S_{Total} = 0$ $[(12\text{-TMC})Co^{III}O_2^{2-}]^+$ electronic structure corresponds to the lowest-energy configuration for **1** and is significantly more stable than any other configuration. The DFT-calculated geometric and electronic structures of **1** are consistent with those of the X-ray diffraction, Co K-edge XAS, and rR data, which are consistent with a $Co^{III}O_2^{2-}$ species. The ^1H NMR spectrum of **1** does not show a paramagnetic shift over a range from −100 to 300 ppm, which indicates a $S_{Total} = 0$ in **1**, also consistent with the DFT results. It is of interest to note that all of the end-on O_2-bound species converge to the $Co^{II}O_2^-$ electronic configuration and so does the high-spin side-on O_2-bound species. Only the low-spin $S_{Total} = 0$, side-on-bound species has a $Co^{III}O_2^{2-}$ ground state, consistent with the optical and X-ray spectroscopy data.[43]

---

(42) The configurations are the side-on- and end-on-bound forms of $Co^{II}(S = 3/2){-}O_2^-(S = {}^1/_2)$, $Co^{III}(S = 2){-}O_2^{2-}(S = 0)$, $Co^{III}(S = 1){-}O_2^{2-}(S = 0)$, $Co^{II}(S = {}^1/_2){-}O_2^-(S = {}^1/_2)$, $Co^{II}(S = {}^3/_2){-}O_2^-(S = -{}^1/_2)$, $Co^{III}(S = 0){-}O_2^{2-}(S = 0)$, $Co^{II}(S = {}^1/_2){-}O_2^-(S = -{}^1/_2)$.

(43) The bond distances and Mulliken spin densities on the intermediate-spin $S_{Total} = 1$ species indicate a mixed $Co^{III}O_2^{2-}/Co^{II}O_2^-$ character in the ground state.

Table 2. Selected DFT Parameters for $[(12\text{-TMC})CoO_2]^+$

		end-on $S_{Total} = 0$	end-on $S_{Total} = 1$	end-on $S_{Total} = 2$	side-on $S_{Total} = 0$	side-on $S_{Total} = 1$	side-on $S_{Total} = 2$
ΔE (kcal/mol)[a]		0	−1.3	6.6	−13.6	−5.1	6.5
structural parameters	Co−O	1.80	1.79	2.1	1.88	1.86	2.07
	O−O	1.35	1.35	1.34	1.44	1.37	1.33
	Co−N (N′)[b]	2.06 (2.11)	2.06 (2.12)	2.14 (2.20)	2.02 (2.05)	2.07 (2.26)	2.13 (2.19)
spin density[c] of Co, O_2		0.6, −0.6	1.3, 0.6	2.6, 1.2	0, 0	1.6, 0.4	2.7, 1.2

[a] The ΔE is calculated as $E - E_{\text{end-on}, S_{Total}=0}$. [b] The Co−N (N′) distances are the average of two trans Co−N bonds. [c] The Mulliken spin densities for Co and O_2 are shown (the spin densities on both O atoms have been added to represent O_2).

Table 3. Selected DFT Parameters for $[(14\text{-TMC})CoO_2]^+$

		end-on $S_{Total} = 0$	end-on $S_{Total} = 1$	end-on $S_{Total} = 2$	side-on $S_{Total} = 0$	side-on $S_{Total} = 1$	side-on $S_{Total} = 2$
ΔE (kcal/mol)[a]		0	−4.1	0.52	−5.1	−0.5	1.0
structural parameters	Co−O	1.85	1.84	1.87	1.90	1.87	2.03
	O−O	1.35	1.35	1.33	1.42	1.38	1.36
	Co−N (N′)[b]	2.07 (2.18)	2.08 (2.17)	2.14 (2.25)	2.08 (2.13)	2.15 (2.31)	2.13 (2.19)
spin density[c] of Co, O_2		−0.5, 0.5	1.3, 0.7	2.6, 1.1	0, 0	1.8, 0.1	2.7, 1.1

[a] The ΔE is calculated as $E - E_{\text{end-on}, S_{Total}=0}$. [b] The Co−N (N′) distances are the average of two trans Co−N bonds. [c] The Mulliken spin densities for Co and O_2 are shown (the spin densities on both O atoms have been added to represent O_2).

3.3.2. $[(14\text{-TMC})CoO_2]^+$. Spin-unrestricted DFT calculations were performed on a $[(14\text{-TMC})CoO_2]^+$ moiety, which was obtained by modifying the crystal structure of the $[(14\text{-TMC})Co(acac)]^{3+}$ complex. Similar to the $[(12\text{-TMC})CoO_2]^+$ calculations above, six ground-state configurations were achieved for $[(14\text{-TMC})CoO_2]^+$ with a combination of starting end-on- and side-on-bound geometries with spin states of $S = 0$, 1, and 2. The energies and structural parameters of these six configurations are shown in Table 3. In contrast to the $[(12\text{-TMC})CoO_2]^+$ calculations, in which the side-on-bound $S_{Total} = 0$ was significantly more stable than any other species, the energies of the six $[(14\text{-TMC})CoO_2]^+$ species differ by at most ~6 kcal/mol. Thus, the energies cannot be used to distinguish between the different electronic configurations in $[(14\text{-TMC})CoO_2]^+$.

The paramagnetic shift observed in the ^1H NMR spectrum of **2** is consistent with an $S = 1$ ground state (see the Supporting Information).[44] On the basis of the NMR data, either the end-on- or side-on-bound $S_{Total} = 1$ species corresponds to the true ground state of **2**. DFT calculations show that the end-on-bound $S_{Total} = 1$ species converges to a $Co^{II}(S = {}^1/_2)-O_2(S = {}^1/_2)$ (ferromagnetically coupled) ground state, while the side-on-bound $S_{Total} = 1$ species converges to a $Co^{III}(S = 1)-O_2(S = 0)$ ground state. The XAS data presented in Figure 1 clearly show that **2** is a Co^{III} species and thus confirm that the correct ground state is $Co^{III}(S = 1)-O_2(S = 0)$.[45]

The optimized geometry for **2** in the side-on-bound $Co^{III}(S = 1)-O_2(S = 0)$ form has two Co−O bonds at 1.87 Å, two Co−N bonds at 2.15 Å, and two elongated Co−N bonds at 2.31 Å, indicating a significant distortion in the 14-TMC ring. This distortion is consistent with the EXAFS analysis (section 3.2 and Scheme 2). Note that the significant elongation of the two Co−N bonds in **2** (2.3 Å is still a bond) is consistent with a distribution of the ligand field at the Co center. This ligand-field distribution leads to stabilization of the intermediate Co^{III} $S = 1$ species. In contrast, most six-coordinate Co^{III} complexes have an $S = 0$ or 2 ground state.

Scheme 2. DFT-Calculated Nearest-Neighbor Distances for **1** (Top) and **2** (Bottom)

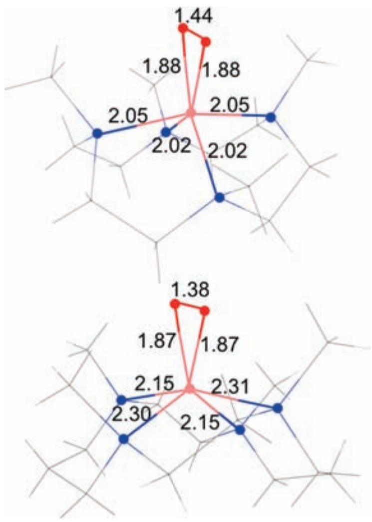

4. Discussion

4.1. Electronic Structures of $[Co(12\text{-TMC})O_2]^+$ and $[(Co(14\text{-TMC})O_2]^+$. **1** and **2** are mononuclear O_2-bound Co complexes formed by the addition of excess H_2O_2 to their starting Co^{II} analogues, $\mathbf{1_{pre}}$ and $\mathbf{2_{pre}}$, respectively, in the presence of a base. Understanding the geometric and electronic structures of **1** and **2** is an important step in our overall understanding of the $M-O_2$ bonding at biological metal centers. In this study, the geometric and electronic

---

(44) Note that in an earlier publication **2** was assigned a $S = 2$ ground state based on the observation of paramagnetic NMR data.[17] Recent NMR data indicate that the previous assignment was erroneous, owing to the presence of extraneous contamination.

(45) Note that the calculated energy of $Co^{III}(S = 1)-O_2(S = 0)$ is higher than that of the $Co^{III}(S = 0)-O_2(S = 0)$ species by 4.6 kcal/mol. However, the NMR data clearly show that **2** is paramagnetic, excluding the possibility that **2** is $Co^{III}(S = 2)-O_2(S = 0)$.

structures of **1** and **2** have been investigated using Co K-edge and EXAFS techniques coupled with DFT calculations. A comparison of the Co K-edge XAS spectra of **1** and **2** to $\mathbf{1}_{\mathbf{pre}}$ and $\mathbf{2}_{\mathbf{pre}}$, respectively, shows that both **1** and **2** are Co^{III} complexes. NMR data show that **1** is diamagnetic, while **2** is paramagnetic with $S = 1$. Together, these data reveal that the electronic structures of **1** and **2** have $Co^{III}(S = 0){-}O_2^{2-}(S = 0)$ and $Co^{III}(S = 1){-}O_2^{2-}(S = 0)$ ground states, respectively. EXAFS analyses of **1** and **2**, coupled with the crystal structure of **1**, demonstrate that both are side-on-bound $Co^{III}O_2^{2-}$ species. The experimental data coupled with DFT calculations show that the four Co−N bonds in **1** are equidistant at ∼2.0 Å from the Co center. In contrast, **2** has a distorted ligand environment with two Co−N bonds at 2.10 Å and two elongated Co−N distances (not observed in EXAFS). DFT calculations show that these two Co−N bonds are at ∼2.31 Å and are trans to each other. This alleviates the steric hindrance posed by the methyl groups and allows for the side-on binding of the O_2 group. Therefore, the 14-TMC ring in **2** undergoes significant distortion to accommodate O_2^{2-} to bind in a side-on fashion, which leads to a decrease in the ligand field strength at the Co center and stabilizes its intermediate-spin $S = 1$ ground state.

4.2. Correlations between NiO_2 and CoO_2 Complexes. An interesting contrast is observed between the O_2-bound Co and Ni complexes of 12-TMC and 14-TMC. Both **1** and $[(12\text{-TMC})NiO_2]^+$ have a side-on O_2-bound low-spin $M^{III}O_2^{2-}$ (M = Co and Ni) ground state. However, while **2** has a side-on O_2-bound $S = 1$ $Co^{III}(S = 1){-}O_2^{2-}(S = 0)$ ground state, $[(14\text{-TMC})NiO_2]^+$ has an end-on O_2-bound $S = {}^1/_2$ $Ni^{II}(S = 1){-}O_2^{-}(S = {}^1/_2)$ ground state. This difference is best seen in the comparison of the Ni and Co K-edge XAS data of the four complexes, as shown in Figure 3. On going from $[(12\text{-TMC})NiO_2]^+$ to $[(14\text{-TMC})NiO_2]^+$ (Figure 3B), the edge shifts down by 1.8 eV, clearly indicating a dramatic decrease in the charge in $[(14\text{-TMC})NiO_2]^+$ (i.e., Ni^{III} to Ni^{II}).[46] In addition, Ni K-edge EXAFS analysis revealed that in contrast to $[(12\text{-TMC})NiO_2]^+$, which has two short Ni−O bonds, $[(14\text{-TMC})NiO_2]^+$ has one Ni−O bond. DFT calculations have suggested that the 14-TMC ligand with the four *cis*-methyl groups[47] posed a strong steric hindrance to the binding of O_2 in a side-on fashion and only allowed for a relatively hindrance-free end-on binding mode with a $Ni^{II}O_2^{-}$ electronic configuration. In contrast, in the 12-TMC case, the omission of two ring carbon atoms constrained the ring, leading to an open conformation. This allowed facile side-on binding of O_2, forming a $Ni^{III}O_2^{2-}$ species. In contrast to the Ni systems, the similarity in the Co K-edge energies for **1** and **2** (Figure 3A) shows that both are Co^{III} species, and the EXAFS data show that both have side-on-bound $Co^{III}O_2^{2-}$ structures. Thus, despite the steric hindrance posed by the 14-TMC ring, O_2 assumes a side-on binding mode to Co in **2**, and to relieve the steric constraints, the 14-TMC ring distorts, as observed by experimental and DFT calculations (see section 3.2).

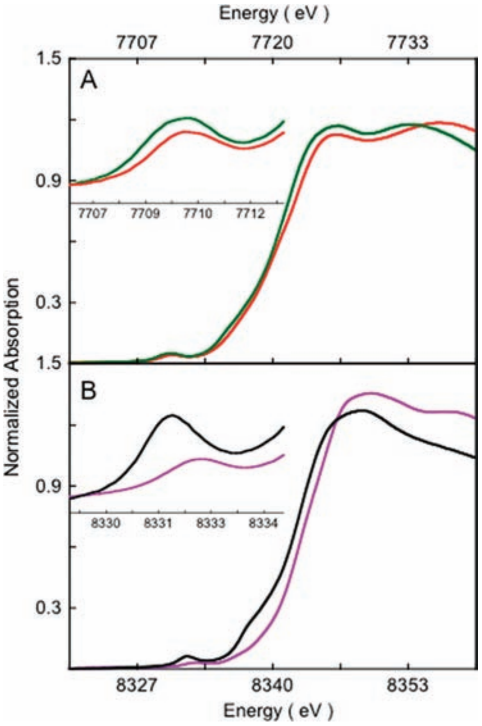

Figure 3. Comparison of the XAS pre-edge and edge shifts: (A) Co K-edge for **1** (red line) and **2** (green line); (B) Ni K-edge for $[(12\text{-TMC})NiO_2]^+$ (purple line) and $[(14\text{-TMC})NiO_2]^+$ (black line). Insets show the expanded preedge region.

To understand this difference in bonding of O_2 to Co and Ni in the 14-TMC case, the energy contributions of the different factors that drive side-on versus end-on bonding were evaluated. The conversion of an end-on-bound $M^{n+}O_2^{-}$ to side-on-bound $M^{(n+1)+}O_2^{2-}$ is affected by different energy terms resulting from (a) the oxidation of M^{n+}, (b) the reduction of O_2^{-}, (c) the potential change in exchange stabilization between the M^{n+} and O_2^{-} spin systems, (d) the differences in bonding, and (e) destabilization due to steric factors. The differences in these energy terms were estimated for the O_2^{n-}-bound Ni and Co complexes of 14-TMC. To evaluate factor a, DFT geometry optimizations were performed on end-on-bound $[(14\text{-TMC})Ni^{II}O_2^{-}]^+$ and $[(14\text{-TMC})Co^{II}O_2^{-}]^+$ and the vertical energy changes upon oxidation of these Ni^{II} and Co^{II} species were calculated.[48] The calculations show that oxidation of the Co^{II} species is 11.5 kcal/mol more favorable relative to the Ni^{II} species. The relative contribution of factor b is similar in both the Co and Ni cases and can be omitted from consideration. The calculated exchange stabilization in $[(14\text{-TMC})Ni^{II}O_2^{-}]^+$ is higher than that in $[(14\text{-TMC})Co^{II}O_2^{-}]^+$ by 1.8 kcal/mol.[49] On going from an end-on to a side-on binding mode of O_2, both the Co and Ni species gain an additional M−O bond. A comparison of the Mulliken populations of the valence metal orbitals involved in bonding with O_2^{2-} shows only minor *relative* changes on going from the Ni to Co complex (see

---

(46) Sarangi, R.; Dey, M.; Ragsdale, S. W. *Biochemistry* **2009**, *48*, 3146–3156.

(47) *FEFF* fits to the EXAFS data were consistent with all four methyl groups cis to the O_2 binding side.

(48) The calculations were performed in the appropriate spin states and were checked to confirm that the vertical oxidation only affected the metal center.

(49) The exchange stabilization energy was obtained from the optimized energies of the high- and low-spin states of $[(14\text{-TMC})Ni^{II}O^{2-}]^+$ and $[(14\text{-TMC})Co^{II}O^{2-}]^+$.[50,51]

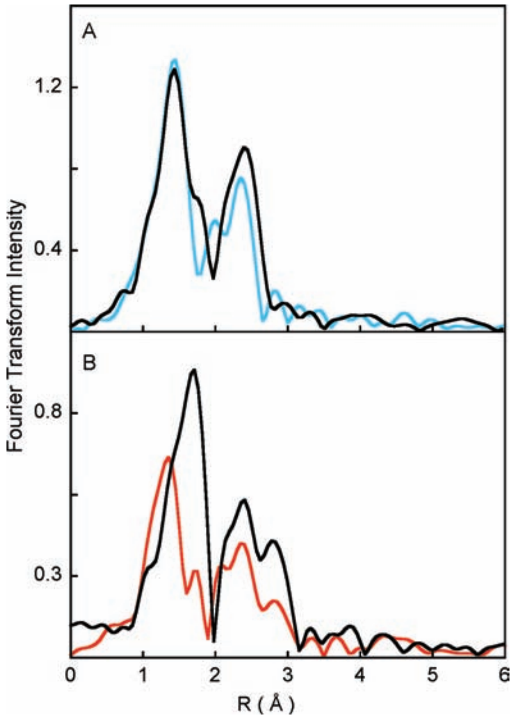

Figure 4. Comparison of the nonphase-shift-corrected Fourier transforms for (A) **1** (light-blue line) and $[(12\text{-TMC})NiO_2](ClO_4)$ (black line) and (B) **2** (red line) and $[(14\text{-TMC})NiO_2](ClO_4)$ (black line).

the Supporting Information) and can also be omitted from consideration. Thus, the Co species prefers to be in the side-on $M^{III}O_2^{2-}$ configuration by ~13.3 kcal/mol relative to the Ni species. The significant stability of the Co^{III} oxidation state relative to the Ni^{III} oxidation state overcomes the steric hindrance posed by the four *cis*-methyl groups in $[(14\text{-TMC})CoO_2]^+$, leading to a distorted 14-TMC ring and a side-on O_2-bound Co^{III} complex. This difference can be clearly seen in the comparison of the Fourier transforms of the EXAFS data of the Ni/Co and 12- and 14-TMC complexes (Figure 4). The first-shell intensities of the two 12-TMC complexes are very similar, while a decrease in the intensity is seen on going from $[(14\text{-TMC})NiO_2]^+$ to $[(14\text{-TMC})CoO_2]^+$, indicating an overall decrease in the first-shell coordination due to the weakening of two Co−N bonds.

In contrast to the 14-TMC systems with steric interactions between the four *cis*-methyl groups, in the steric-free $[(12\text{-TMC})NiO_2]^+$ case, the side-on-bound $Ni^{III}O_2^{2-}$ form is 8.7 kcal/mol more stable than the end-on O_2-bound $Ni^{II}O_2^-$ form. Combining this with the calculated relative stability of the Co^{III} case, the steric constraints posed by the 14-TMC ring can be bracketed, as higher than ~8.7 kcal/mol but less than ~22 kcal/mol.

In summary, for both the $[CoO_2]^+$ and $[NiO_2]^+$ systems, end-on O_2 binding leads to stabilization of a $[M^{II}O_2^-]^+$ electronic structure, while side-on O_2 binding leads to the formation of a $[M^{III}O_2^{2-}]^+$ species. The sterics of the *cis*-14-TMC chelate contribute to the geometry of O_2 binding, and therefore the electronic structure for the $[Ni(14\text{-TMC})O_2]^+$ complex results in an end-on-bound $Ni^{II}O_2^-$ complex. However, the higher thermodynamic driving force for oxidation of Co^{II} overcomes this steric constraint, resulting in stabilization of a side-on-bound $Co^{III}O_2^{2-}$ electronic structure in the 14-TMC complex.

Acknowledgment. SSRL operations are funded by the Department of Energy, Office of Basic Energy Sciences. The SSRL Structural Molecular Biology program is supported by the National Institutes of Health, National Center for Research Resources, Biomedical Technology Program, and Department of Energy, Office of Biological and Environmental Research. The research was supported by NRF/MEST of Korea through the CRI and WCU (R31-2008-000-10010-0) Programs (to W.N.) and by the NIH DK31450 (to E.I.S). This publication was made possible by Award Number P41 RR001209 from the National Center for Research Resources (NCRR), a component of the National Institutes of Health (NIH). Its contents are solely the responsibility of the authors and do not necessarily represent the official view of NCRR or NIH.

Supporting Information Available: DFT geometry-optimized coordination of **1** and **2** in *xyz* format, DFT-calculated molecular orbital contour plots representing the Mulliken spin density of the valence Co d orbitals in end-on- and side-on-bound $[(12\text{-TMC})CoO_2]^+$ and $[(14\text{-TMC})CoO_2]^+$, and the ^1H NMR spectrum of **2**. This material is available free of charge via the Internet at http://pubs.acs.org.

---

(50) Noodleman, L. *J. Chem. Phys.* **1981**, *74*, 5737–5743.
(51) Noodleman, L.; Davidson, E. R. *Chem. Phys.* **1985**, *109*, 131–138.